

Neutral Defects in SrTiO₃ Studied with Screened Hybrid Density Functional Theory

Fedwa El-Mellouhi,^{1,*} Edward N. Brothers,^{1,†} Melissa J. Lucero,² and Gustavo E. Scuseria^{2,3,4}

¹*Chemistry Department, Texas A&M University at Qatar,*

Texas A&M Engineering Building, Education City, Doha, Qatar

²*Department of Chemistry, Rice University, Houston, Texas 77005-1892*

³*Department of Physics and Astronomy, Rice University, Houston, Texas 77005-1892*

⁴*Chemistry Department, Faculty of Science, King Abdulaziz University, Jeddah 21589, Saudi Arabia*

The properties of neutral defects in SrTiO₃ are calculated using the screened hybrid density functional of Heyd, Scuseria, and Ernzerhof (HSE). The formation energies, the crystal field splittings affecting the SrTiO₃ band structure, as well as the relaxation geometries around each defect are discussed. Oxygen vacancies introduced in SrTiO₃ are found to cause a small tetragonal elongation of the lattice along the *z*-axis. The resulting conduction band minimum electron effective masses deviate from the bulk values and support the proposal of enhanced electron mobility along the direction of the compressive strain. The locations of the various defect bands within the SrTiO₃ gap are estimated without introducing any post-hoc corrections, thus allowing a more reliable comparison with experiment.

PACS numbers: 71.15.Mb, 71.15.Nc, 71.55.i, , 71.55.-Ht

I. INTRODUCTION

The properties of point defects in metal oxides and their superlattices have been an area of recent interest, and have been investigated using increasingly precise and sophisticated experimental methods.[1, 2] Optical experiments can determine differences between sharp photoluminescence peaks with meV precision;[3] this can be used to determine the different *types* of defects, but the chemical identity of a point defect or defect complexes remains difficult to obtain. Electronic structure methods have been used to obtain the formation energies and the location of defect levels within the gap to identify the source the photoluminescence peaks.[4, 5] However, first principles calculation of defects in complex systems suffer from several limitations.[6] The long-range interaction between defects in neighboring cells, an artifact of periodic boundary conditions (PBC), can affect relaxation around a defect. [7] Also, correcting the spurious interaction between charged defects[8, 9] and the introduced compensating background charge is an area of ongoing interest. Furthermore, there is a well-known underestimation of band gaps when calculations using the local spin density approximation[10] (LSDA) of density functional theory (DFT) are performed; while it is possible to apply a post-hoc correction to the gap and get good results for uniform solids,[11] it is less obvious how comparable to experiment the result of this practice is when applied to the location of the defect levels. More advanced semilocal density functionals perform better but still generally underestimate the band gap. [12]

Some of these limitations may be overcome via post-DFT or hybrid DFT calculations, which often give band

gaps closer to experiment. [12] Band gap accuracy generally implies efficacy in modeling defect structures; for example, a recent comparison of semilocal and hybrid density functional theory (DFT) calculations showed that there is a strong correlation between the calculated valence band width (VBW) and defect formation energies.[13] Accurate VBW values obtained with the Heyd-Scuseria-Ernzerhof screened hybrid functional[14] (HSE) lead to point defect formation energies and energy levels in close agreement with experiment for elemental and binary nonmetals. [15–17] These findings are encouraging because (unlike semilocal functionals) screened hybrid functionals require no post-DFT correction of the band gap and provide excellent lattice parameters in addition to other bulk properties.[18–21] In studies of cubic SrTiO₃(STO)[22–25] and other perovskites,[23, 26–28] HSE has been shown to perform well for band gaps, spin-phonon effects, and numerous structural effects, including strain, bulk moduli, octahedral angles tilts and rotations amongst others. Recently, a regular and hybrid density functional study on many perovskites [29] has highlighted the relevance of anharmonic corrections to lower the octahedral rotation and tilt angles. The anharmonic correction was 0.15° for all compounds except STO for which the correction was 0.8°. For methods containing 25% HF mixing, namely PBE0 and PBEsol0, the uncorrected angles in SrTiO₃ were already close to experiment; applying the anharmonic correction lead to too small angles. HSE belongs to the same family but has a screening parameter $\omega = 0.11$, so it can be thought of as an interpolation between PBE ($\omega = \infty$) and the global hybrid PBE0 ($\omega = 0$). We expect the anharmonic effects correction would lead to HSE octahedral rotations overcorrected to too small angles compared to experiment.

We here present the results of our HSE calculations for the formation energies and band structures of neutral defects in SrTiO₃. This work is motivated by HSE's

* fadwa.el_mellouhi@qatar.tamu.edu

† ed.brothers@qatar.tamu.edu

agreement with experiment in the calculation of many of the electronic, structural and elastic properties in cubic SrTiO₃ [22, 23] and other metal oxides. [26] It is worth noting that the direct and indirect band gaps as well as VBW are in excellent agreement with experiment (see table I) compared to the results from LSDA and B3PW [30], which were previously used to study point defects in SrTiO₃. We focus on the various neutral vacancies in SrTiO₃, such as the oxygen (V_O^0), strontium (V_{Sr}^0) and titanium vacancies (V_{Ti}^0), as well as on the effect of doping STO with La (La_{Sr}).

II. COMPUTATIONAL METHODS

All calculations included in this manuscript were performed using the development version of the GAUSSIAN suite of programs, [31] with periodic boundary conditions (PBC) [32] used throughout. The functionals applied in this work include the generalized gradient approximation of Perdew, Burke and Ernzerhof [33, 34] (PBE) and HSE. [14] The Def2- [35] series of Gaussian basis sets were optimized following our procedure, described in Ref. 22. We use the notation SZVP to differentiate these optimized PBC basis sets from the molecular Def2-SZVP basis sets. Strontium has the inner-shell electrons replaced with smallcore pseudopotentials, while for oxygen and titanium atoms we utilize all electron basis sets. SZVP basis offers a good compromise between computational efficiency and high accuracy for electronic and structural properties of bulk SrTiO₃. [22] The use of SZVP basis set with HSE screened hybrid functional (HSE/SZVP) imposes limitations on the size of the supercell that can be efficiently computed, so a STO supercell of $2 \times 2 \times 2$ (40 atoms) was used with a dense k -point mesh of $6 \times 6 \times 6$ which included the Γ point. Calculations with larger supercells of $2 \times 3 \times 3$ (90 atoms) with the same density of k -points were performed in order to discuss the importance of defect self-interactions and the effect of varying the defect concentration on the electronic properties of STO. The pruned integration grid for DFT employed was (99,590), which corresponds to the Gaussian option "ultrafine". The remaining numerical settings in GAUSSIAN were left at the default values, *e.g.*, geometry optimization threshold was set to 450×10^{-6} hartrees/bohr, SCF convergence was set to "tight". Unless otherwise noted, crystal structures for chemical potential calculations on SrO, TiO, Ti₂O₃, and Ti₂O were downloaded as CIF files from the ICSD. [36] All structures are fully relaxed (optimized) unless otherwise noted.

III. RESULTS AND DISCUSSION

A. Vacancy Formation Energy Calculations

The calculations of neutral defect formation energies are based upon the formalism of Zhang and Northrup. [41]

TABLE I. Comparison of properties of bulk STO relevant to defect formation from our work, previous computational studies, and experiment. Our HSE/SZVP band gaps and valence band widths (VBW) are closer to experiment than the semilocal LSDA and the global hybrid B3PW results.

	LSDA ^a	B3PW ^a	HSE ^b	Exp.
Direct gap (eV)	2.36	3.96	3.59	3.75 ^c
Indirect gap (eV)	2.04	3.63	3.20	3.25 ^c
VBW (R→R)(eV)	4.77	6.47	5.0	5.0 ^c
a_0 (Å)	3.86	3.90	3.89	3.89 ^d , 3.90 ^e
B(GPa)	214	177	204	179

^a Ref. 37

^b Ref. 22

^c Ref. 38

^d Ref. 39.

^e Ref. 40.

These values are generated using the equation

$$E_f = E_T - [E_T(\text{perfect}) - n_{Sr}\mu_{Sr} - n_{Ti}\mu_{Ti} - n_O\mu_O] \quad (1)$$

where E_T and $E_T(\text{perfect})$ are the calculated total energies of the supercells containing the point defect and the perfect bulk host materials, respectively. The number of each element removed from the perfect supercell is represented by n_x , while μ_x corresponds to the atomic chemical potentials in an SrTiO₃ crystal. Given the assumption that SrTiO₃ is always stable, the chemical potentials of these elements can vary with the following restriction:

$$\mu_{Sr} + \mu_{Ti} + 3\mu_O = \mu_{SrTiO_3(bulk)} \quad (2)$$

Atomic chemical potentials vary according to the sample composition and cannot be determined exactly. However, they can be varied to cover the whole phase diagram of SrTiO₃, by splitting into SrO, TiO, Ti₂O₃, and Ti₂O bulk phases. Hence, the calculated formation energies for the neutral point defects vary according to equilibrium positions; an example of this is O-rich versus O-poor points on the phase diagram. The calculated enthalpies of formation in idealized materials (non-relaxed structures) for phases containing Sr, Ti and O are summarized in Table II, and are compared to previous LSDA calculations [42] and experiment. [43]

As a general trend, the formation enthalpies computed with HSE are close to the results from semilocal functionals LSDA and PBE (from this work), although the HSE values are slightly higher. The only exception is SrO, where both HSE and PBE tend to overestimate the formation enthalpies to the same extent, exceeding the LSDA values.

The formation energies of vacancy defects in STO as a function of its composition are plotted in Figure 1 with the points A to G [44] based on the phase diagram in

TABLE II. Calculated enthalpies of formation in eV/atom for idealized materials for phases containing Sr, Ti and O compared to previous LSDA calculations and experiment.

	HSE	PBE	LSDA ^a	Exp. ^b
TiO ₂	-3.92	-3.75	-3.76	-3.24
Ti ₂ O ₃	-3.74	-3.60	-3.63	-3.15
TiO	-2.99	-2.95	-3.04	-2.81
SrO	-4.00	-3.90	-3.36	-3.07

^a Ref. 42

^b Ref. 43

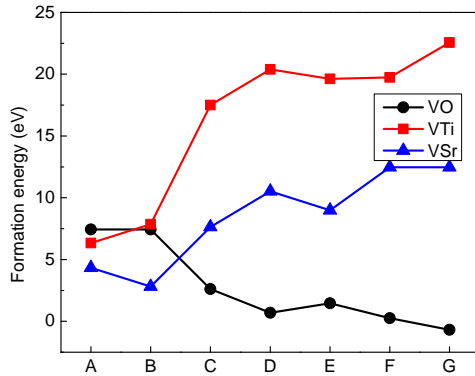


FIG. 1. (Color online) Defect formation energies of isolated neutral vacancies in STO at each equilibrium point based upon the phase diagram detailed in the text.

Ref. 42. The plot shows that HSE's formation energies show a similar dependence on the chemical potentials as was observed for the LSDA results of Ref. 42. However, both V_{Ti}^0 and V_{Sr}^0 curves are shifted to higher formation energies, while the V_{O}^0 curve is slightly shifted downwards compared to the LSDA spectrum. At point A, V_{O}^0 has the lowest formation energy followed by V_{Ti}^0 and V_{Sr}^0 . At point B, V_{Sr}^0 remains the most stable but V_{O}^0 becomes more stable than V_{Ti}^0 contrary to the LSDA predictions. Under low partial pressures of oxygen (O-poor conditions corresponding to points C to G), V_{O}^0 vacancies form more easily and dominate the spectrum while the formation energies of V_{Ti}^0 and V_{Sr}^0 keep increasing.

A quantitative comparison with previously published calculations using the same cell size formation energies [30, 42, 45] available at point B (oxygen rich conditions) reveal several issues of interest.

- For V_{O}^0 , the semilocal functional PW91[45] yields a formation energy of 8.56 eV, the global hybrid B3PW [30] predicted a higher formation energy of 8.74 eV, while LSDA [42] gave a lower value at 7.95 eV. Our HSE value is the lowest among these, yielding a formation energy of 7.43 eV. This decrease in the V_{O}^0 formation energy is one of the factors leading to a strong competition with V_{Ti}^0 (see below).

- For V_{Ti}^0 , the semilocal functional LSDA [42] yields a formation energy of 5.7 eV making it far more stable than V_{O}^0 . In contrast, with HSE we predict that $E_f = 7.86$ eV meaning that V_{Ti}^0 becomes less stable than V_{O}^0 .
- V_{Sr}^0 remains the most stable defect under these conditions, with HSE providing a value of 2.81 eV compared to the 1.7 eV from LSDA.

Overall, the quantitative formation energies differences between our HSE results and previous LSDA results are substantial. These might originate from the enhanced accuracy we gain with HSE in the calculated valence band width (VBW) and band gap of bulk SrTiO₃ (see table I) identified in Ref. 13 to reflect an enhanced precision in the defect formation energies.

It is also worth mentioning size effects. The formation energy of V_{O}^0 at point B in a larger supercell of 90 atoms, giving a 1.8% V_{O}^0 concentration, is 7.66 eV, which is 0.2 eV higher than the value obtained with the smaller supercell.

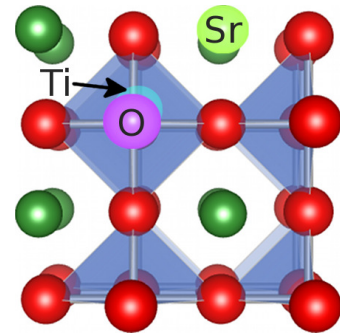


FIG. 2. (Color online). Ideal, crystalline SrTiO₃, as observed from the 100 face, where the oxygen anions are in red, the strontium cations are in green and the titanium cations are in blue. Magenta, yellowish and cyan circles highlight the locations of the isolated V_{O}^0 , V_{Sr}^0 and V_{Ti}^0 defects, respectively.

B. Isolated Vacancies: Relaxation Effects

Isolated, neutral defects have been introduced into the crystal structure of cubic STO by removing one atom of either O, Sr or Ti, respectively, as depicted in Figure 2. The structure was then fully relaxed using HSE/SZVP. Figure 3 illustrates the major displacements in each of the defect structures, namely V_{O}^0 , V_{Sr}^0 and V_{Ti}^0 , relative to the idealized crystal. Distance *decreases* are depicted by black arrows, while *increasing* lengths are denoted by yellow arrows. In each case, the magnitude of displacement is implied by the size of the arrows: larger/thicker arrows indicate greater deviation from the defect-free structure.

A 4% V_{O}^0 vacancy was created by removing one oxygen (Figure 3-a) from a $2 \times 2 \times 2$ cell, inducing small, asymmetric bond length changes throughout the cell and an

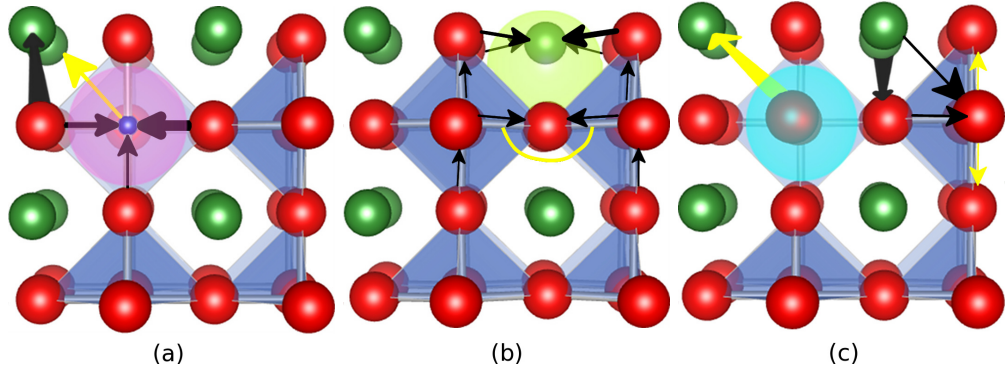


FIG. 3. (Color online). Relaxed SrTiO_3 with a single isolated vacancy. Each structure is in the 100 orientation and the location of the vacancy is noted. The distortions induced by V_{O}^0 , V_{Sr}^0 and V_{Ti}^0 are highlighted (a), (b) and (c), respectively. Oxygen anions are red, Sr cations are green, and Ti cations are blue.

overall decrease in volume relative to the crystal. At the vacancy, the remaining O-Ti bonds all contract but to different extents. Near the vacancy, oxygens move toward nearby strontium, inducing O-Sr bond contractions of up to 5.66 pm. Further from the vacancy, in the regions of the cell behind the defect (and the plane of the figure), strontium appears to migrate inward, toward the vacancy, causing the more distant O-Sr bonds to lengthen by as much as 6.05 pm.

The V_{O}^0 structure contracts, and undergoes a tetragonal distortion where the lattice parameters are $a = 3.879$ and $b = c = 3.890$ Å, compared to the 3.902 Å in the crystal. High concentration of oxygen vacancies were identified to be responsible of a similar tetragonal distortion reported experimentally [3] in STO doped with La. Worth noting that with HSE/SZVP, we are able to capture this small tetragonal distortion corresponding to a c/a ratio of 1.0028. This distortion was also observed in previous LDA calculations [46] for supercells of the same size, but the c/a ratio was not reported.

As seen from Figure 3-b, the atomic relaxation around the V_{Sr}^0 induce staggered bond lengths (vertically) and a general contraction of O-Sr bonds, with the large decrease being 1.55 pm, smaller than those observed for O-Sr in the presence of an oxygen vacancy. The alternating distances cause the linear Ti-O-Ti angle to decrease to 173.9° . Again, the defect structure contracts, with all lattice parameters decreasing: $a = b = c = 3.880$ Å.

The V_{Ti}^0 structure depicted in Figure 3-c shows the axial oxygens experiencing a 9.2 pm decrease in length, while the medial oxygens move away from the vacancy by 0.6 pm. The Sr-O distances shrink over a range of 1.51 to 5.40 pm. While also asymmetric, these distortions have less of an effect on the cell, with the equilibrium lattice parameters being $a = c = 3.892$ and $b = 3.894$ Å. The a/b ratio here is very small so the structure remains effectively cubic following full relaxation.

In summary, the loss of metallic species results in

smaller volumes with the loss of the larger metal, V_{Sr}^0 , producing greater contraction. Removing the oxygen produces larger deviations from cubic symmetry in addition to overall shrinkage of the unit cell.

C. Isolated Vacancies: Band Structures

The electronic band structure and the projected densities of states (PDOS) of the ideal and nonideal/defect STO supercells (doped with O, Sr and Ti neutral vacancies) are shown in figure 4. To allow a clear comparison between the different systems, the VBM was set as reference for all systems while the Fermi energy is depicted with a solid line. The PDOS are plotted alongside with their corresponding band structure and rescaled in the same way.

For the ideal $2 \times 2 \times 2$ STO supercell the Brillouin zone folds, causing a direct band gap of 3.19 eV. The CBM in the ideal solid is triply degenerate at Γ and composed of a heavy electron band (he), a light electron band (le) and a spin-orbit band (so). The band degeneracy is lifted as we move far from the Γ point towards high symmetry directions X , M and R , giving rise to different values of the electron effective masses m_{he} , m_{le} , m_{so} in each direction. The electronic effective mass for each band i can be computed by the curves of energy versus \vec{k} being fitted to a parabola [47]; \vec{k} is taken from the Γ point up to 0.5% along $\Gamma \rightarrow X$, $\Gamma \rightarrow M$ and $\Gamma \rightarrow R$ paths using the formula:

$$\frac{1}{m} = \frac{2}{\hbar} \frac{d^2 E}{dk^2} \quad (3)$$

We estimate the $\Gamma \rightarrow X$ effective masses, without spin-orbit correction, $m_{he}^{\Gamma \rightarrow X}$ and $m_{le}^{\Gamma \rightarrow X}$ to be $7.3m_e$ and $0.5m_e$ respectively, where m_e is the free electron mass. This agrees well with previous nonrelativistic calculations [23, 47, 48] using LSDA and HSE, which

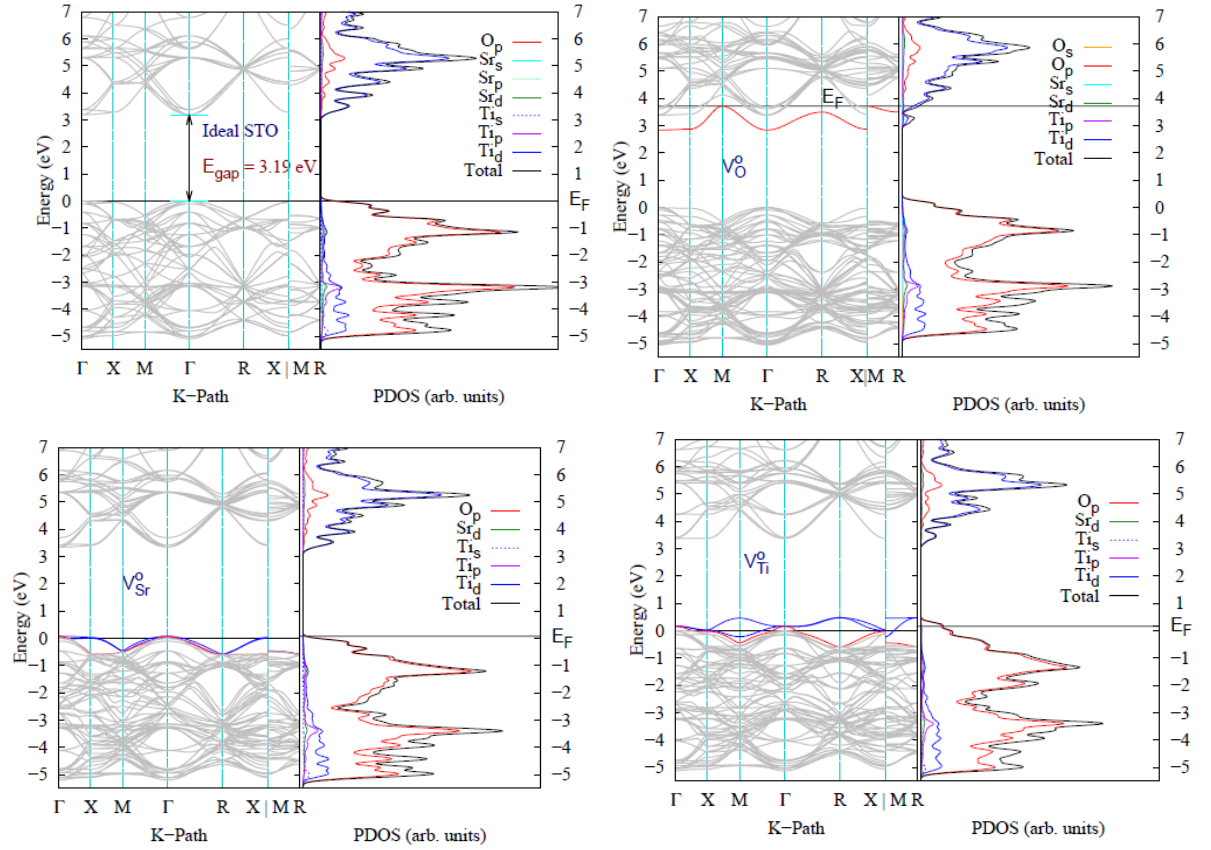


FIG. 4. (Color online). Band structures and PDOS calculated with HSE/SZVP for the $2 \times 2 \times 2$ SrTiO_3 supercell. The top figures represent bulk STO, and V_{O}^0 while the bottom row contains V_{Sr}^0 and V_{Ti}^0 . The Fermi energy E_F is indicated by a solid black line. The red bands indicate the occupied defect bands while the unoccupied defect bands are shown in blue.

predicted *he* masses ranging from 6.1 to $7.3m_e$ and *le* masses of $0.4m_e$. The remaining effective masses are $m_{he}^{\Gamma \rightarrow M} = 1.1m_e$, $m_{le}^{\Gamma \rightarrow M} = 0.8m_e$, $m_{he}^{\Gamma \rightarrow R} = 0.9m_e$ and $m_{le}^{\Gamma \rightarrow R} = 0.7m_e$.

Introducing V_{Ti}^0 into STO, the defect band averaged in the Brillouin zone is located at 0.13 eV above the valence band maximum (VBM) and 3.06 eV below the conduction band maximum (CBM) (see Table III). The defect band has a VB character and is triply degenerate at Γ

with a single band occupied by two electrons, while the upper two bands are empty (see figure 4). The crystal field resulting from the atomic relaxation around V_{Ti}^0 causes the triply degenerate CBM band to split in the following way: the heavy electron band (*he*) is followed by the light electron band (*le*) at 26 meV, while the spin-orbit band (*so*) is located 14 meV higher.

For V_{Sr}^0 , a triply degenerate defect band appears at 0.07 eV above the VBM and 3.27 eV below the CBM at the Γ point. From figure 4, two bands are occupied by four electrons while the upper band is empty. The degeneracy of the defect band is lifted at the X point, where the two occupied band remain degenerate while the unoccupied band is 600 meV higher in energy. The *he* and *le* bands in the CBM remain degenerate while the *so* band is located at 1.5 meV higher in energy mainly because the overall deformation V_{Sr}^0 introduces into the lattice is small.

Introducing V_{O}^0 into STO causes a defect band (DB) populated with two electrons to appear in the gap just below the bulk-like conduction band maximum labelled here as (DCBM), indicating a donor band. The Fermi energy is shifted from the top of the valence band to the maximum of the defect band at the M point fol-

TABLE III. Location of the various defect bands averaged in the Brillouin zone with respect to the conduction band minimum ($\Delta\epsilon_{\text{DB-CBM}}$) and valence band maximum ($\Delta\epsilon_{\text{DB-VBM}}$). Data are for the $2 \times 2 \times 2$ SrTiO_3 supercell computed with HSE/SZVP. Defect formation energies (in eV) at point B (oxidation condition) are reported as well.

	$\Delta\epsilon_{\text{DB-CBM}}$	$\Delta\epsilon_{\text{DB-VBM}}$	E_f
V_{Ti}^0	3.06	0.15	7.86
V_{Sr}^0	3.27	0.07	2.81
V_{O}^0	0.44, 0.40 ^a	2.82, 2.90 ^a	7.43

^a Experimental estimations from Refs. 3 and 49

lowed by the empty conduction band. The CBM conserves the bulk character as it remains empty and triply degenerate (clearly shown in Figure 4) corresponding to the Ti t_{2g} states followed by a doubly degenerate e_g band. The above CBM conservation of degeneracy confirms that the band appearing underneath is a fully occupied non-degenerate defect band. The isosurface of the highest occupied state at the Γ special k-point (Figure 5) shows that the electronic charge density is localized on V_O^0 occupying the Ti dangling bonds.

We calculated the position of the defect state by averaging over the Brillouin zone. We found that the DB is located in average at 0.44 eV below the CBM for the 40 atoms supercell (see table III) and 0.42 eV for the 90 atoms supercell. This could be compared the recent experimental measurements, which place the position of the defect level 0.4 eV below the CBM, causing the blue light photoluminescence of STO at room temperature. [3, 49] In the present calculations, self-defect interaction or the so-called size effects were minimized by keeping the defects neutral, and conserving the same high density of k -point sampling of the Brillouin zone. [50] Nevertheless, simulations using larger supercells and finite size scaling [7] are still needed for a more accurate comparison. As of today's computational resources, a full relaxation of larger supercells using HSE/SZVP and the computational settings used here are computationally very expensive. This defect band seems to be shallower than the one computed with B3PW, which was located 0.79 eV below the CBM. [30] We attribute this to the B3PW functional overestimating the band gaps (indirect gap of 3.6 eV compared to 3.2 eV from experiment). Our HSE-predicted defect level for V_O^0 is deeper than that calculated with LDA; in those calculations the defect band can often not be distinguished from the CBM (resonant band), [46] although in some cases it lies as little as 0.08 eV below the CBM. [42]

The atomic relaxation around V_O^0 leads to a tetragonal distortion of the supercell where $c/a=1.0028$ (see Section IIIB), corresponding to a -0.3% compressive strain along the X axis. This amount of strain is comparable to the values applied experimentally in La doped STO [24] and identified as causing a substantial increase of the electron mobilities (by a factor of 3.3) due to the appearance of light electron effective mass along the strain and the transport direction.

In our calculation, the effective mass $m_{he}^{\Gamma \rightarrow X}/m_e$ along the direction parallel to the compressive strain ($k^{\parallel} = \pi/a(100)$) drops from the bulk value of 7.3 to 0.5 in defective $SrTiO_3$ (see table IV), indicating that the electron mobility increases substantially along the x -axis. However, $m_{he}^{\Gamma \rightarrow X}/m_e$ increases along the $k^{\perp} = \pi/a(010) = \pi/a(001)$ directions (perpendicular to the compressive strain) to 11.0 indicating a reduced electron mobility in these directions. Along $\Gamma \rightarrow M$, the effective masses remain unchanged in the $k^{\parallel} = \pi/a(110) = \pi/a(101)$ containing the strain axis.

D. STO doped with La

The substitution of one Sr atom by a La atom in our $2 \times 2 \times 2$ STO supercell lead to a dopant concentration of 12.5%, which is low enough to be compared to experimental data, [3] where dopant concentrations as high as 15% has been used. The resulting $Sr_{0.875}La_{0.125}TiO_3$ compound relaxes to a cubic structure with lattice parameters $a=b=c=3.893$ Å. This agrees well with experiments [3] which demonstrated that La doping conserves the cubic symmetry, and has a negligible effect on the c -axis lattice parameter.

Figure 6 shows the band structure of $Sr_{0.875}La_{0.125}TiO_3$ for spin up and spin down electrons. For the spin up electrons, the VBM is almost triply degenerate with a very small splitting of 7 meV; this is also the case of the lowest CB, a band which is populated with one extra electron and shows a small band broadening (13 meV). The energy difference between the last VB and the first populated CB is 3.16 eV. The next set of conduction bands, normally located at 200 meV above the CBM in the bulk STO, is split into one band a 172 meV above the CBM followed by a doubly degenerate band 100 meV higher. The visualization of isosurface of the highest occupied state at the Γ special k-point show that the charge density is not localized on the defect site, but rather corresponds to the Ti t_{2g} states. The electronic density of states (not shown) also confirms that CB remains dominated by Ti $3d$ states as it does in the STO bulk phase; La $4d$ starts to contribute to the CBM only at about 2.3 eV above the Fermi energy.

For the spin down electrons (bottom of figure 6) the band structure conserves most of the bulk band characteristics with triply degenerate CBM and VBM, but the band gap is larger than the bulk value, measuring 3.55 eV. The heavy electron effective masses relative to the

TABLE IV. Non-relativistic HSE/SZVP calculated heavy electron effective masses (in units of the free-electron mass m_e) at the conduction maximum along different high-symmetry directions in ideal (m_{he}^{CBM}) and oxygen vacancy doped $SrTiO_3$ (m_{he}^{DCBM}). k^{\parallel} and k^{\perp} represent the parallel and perpendicular plans to the direction of the compressive 100 strain resulting from V_O^0 .

Direction	m_{he}^{CBM}	m_{he}^{DCBM}
$\Gamma \rightarrow X(100)$		
k^{\parallel}	7.3	0.5
k^{\perp}	7.3	11.2
$\Gamma \rightarrow M(110)$		
k^{\parallel}	1.1	1.1
k^{\perp}	1.1	1.1
$\Gamma \rightarrow R(111)$		
	0.9	0.9

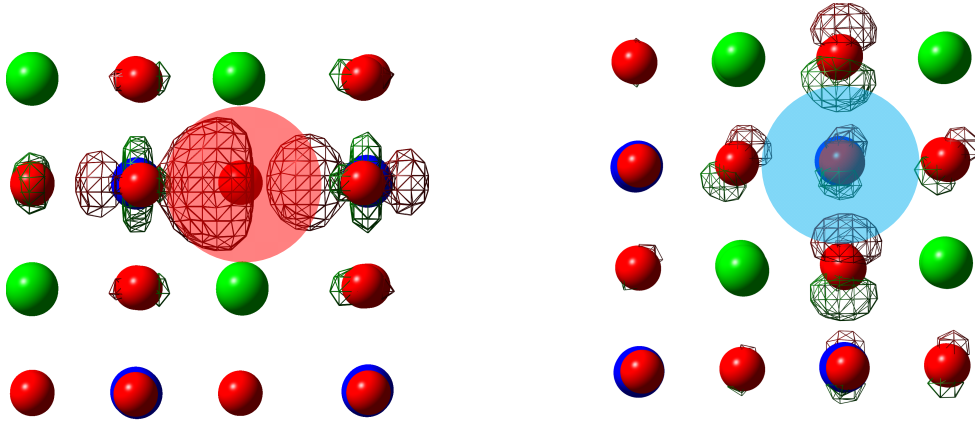


FIG. 5. Isosurface of the highest occupied orbitals viewed along the 100 direction showing (a) orbital localization around (a) V_O^0 (left) V_{Ti}^0 (right).

free electron mass (m_{he}^*/m_e) of the lower band or heavy electron (he) band are isotropic and experience a decrease from the bulk value of 7.3 to 6.8 in the $\Gamma \rightarrow X$ direction, bringing the m_{he}^*/m_e ratio closer to the experimentally measured values [3] of 6-7.1 for 15% La doping. A smaller decrease is observed along the other high symmetry directions.

IV. SUMMARY AND CONCLUSIONS

The structural and electronic properties of point defects V_O^0 , V_{Ti}^0 , V_{Sr}^0 and La_{Sr} in $SrTiO_3$ have been computed using the HSE screened hybrid functional. The crystal field splittings of the conduction and valence bands, resulting from the atomic relaxation around the various defects, were evaluated. HSE is known to give an accurate description of band gap and VBW of $SrTiO_3$, which leads to the assumption it will perform also well the defect energetics, as we have shown here. In fact, the location of the neutral defect bands in the band gap of STO calculated with HSE/SZVP do not suffer from the band gap underestimation problems displayed by semilocal functionals, thus negating the need for further corrections. The wavefunction is localized around V_O^0 and V_{Ti}^0 as shown from the isosurface of highest occupied orbitals in figure 5 and delocalized for the defect states that almost or completely overlap with host bands like V_{Sr}^0 and La_{Sr} . Our calculated defect bands positions are represented schematically in Figure 7; we present the results this way for ease of use and comparison to subsequent works. The location of the defect level in the band gap of STO indicates that V_O^0 is probably at the origin of the blue luminescence of STO, and serves as a double shallow donor under thermal equilibrium. This defect level diagram might serve as a guideline in the interpretation of photoluminescence experiments. [1, 3] For $SrTiO_3$ doped with V_O^0 , the calculated conduction band electron effective

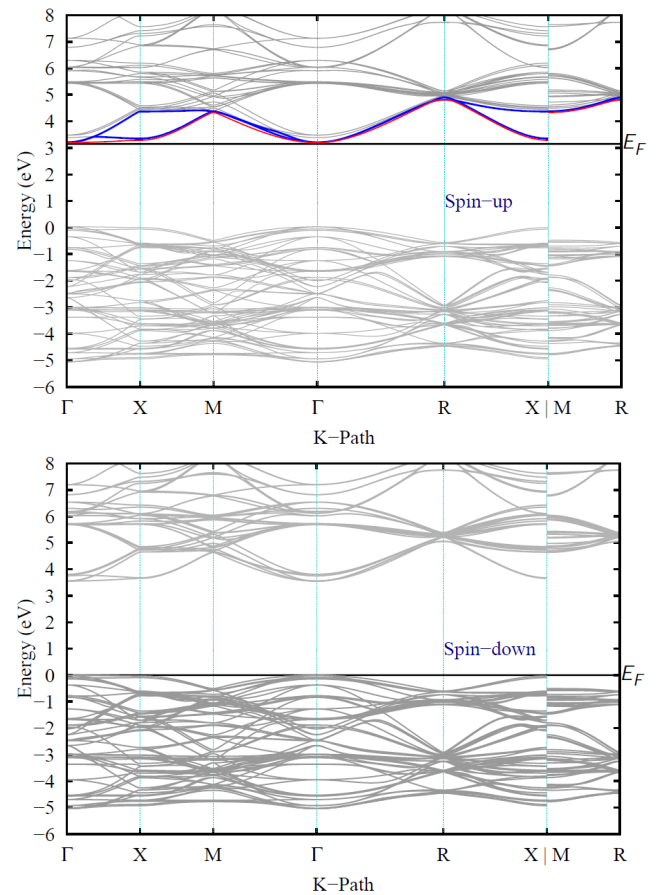


FIG. 6. (Color online) Band structure for spin up (Top) and down (Bottom) electrons in a $2 \times 2 \times 2$ $SrTiO_3$ supercell doped with La. The Fermi energy E_F is indicated by a solid black line. For spin up electrons, one of the triply degenerate bands in the CBM is populated (shown in red) while the remaining empty ones are shown in blue.

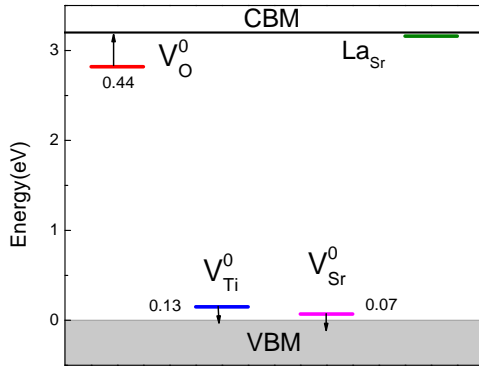


FIG. 7. (Color online) Schematic representation of the location of the defect levels in the band gap of SrTiO_3 calculated with HSE/SZVP. Numbers and arrows refer to the location of the defect band with respect to the nearest bulk-like bands.

tive masses support the proposal of enhanced mobility along the strain directions. [24]

Finally, with its two fixed and unmodified parameters, the HSE functional gave a reliable description of the electronic structure for STO and its defects, in agreement with the findings in Ref. 12 and 51. It would be very interesting to extend the present study for larger supercells followed by the a finite size scaling. This would enable assess the robustness of the present agreement we get with experiment and allow a better comparison by performing double doping with La and V_O^0 .

ACKNOWLEDGMENTS

This work is supported by the Qatar National Research Fund (QNRF) through the National Priorities Research Program (NPRP 08 - 431 - 1 - 076). We are grateful to the Research computing facilities at Texas A&M University at Qatar for generous allocations of computer resources.

-
- [1] Z. Q. Liu, D. P. Leusink, X. Wang, W. M. Lü, K. Gopinadhan, A. Annadi, Y. L. Zhao, X. H. Huang, S. W. Zeng, Z. Huang, A. Srivastava, S. Dhar, T. Venkatesan, and Ariando, *Phys. Rev. Lett.* **107**, 146802 (2011).
 - [2] H. Y. Hwang, Y. Iwasa, M. Kawasaki, B. Keimer, N. Nagaosa, and Y. Tokura, *Nat. Mater.* **11**, 103 (2012).
 - [3] J. Ravichandran, W. Siemons, M. L. Scullin, S. Mukerjee, M. Huijben, J. E. Moore, A. Majumdar, and R. Ramesh, *Physical Review B* **83**, 035101 (2011).
 - [4] J. Chakhalian, A. J. Millis, and J. Rondinelli, *Nat. Mater.* **11**, 92 (2012).
 - [5] J. Chakhalian, J. M. Rondinelli, J. Liu, B. A. Gray, M. Kareev, E. J. Moon, N. Prasai, J. L. Cohn, M. Varela, I. C. Tung, M. J. Bedzyk, S. G. Altendorf, F. Strigari, B. Dabrowski, L. H. Tjeng, P. J. Ryan, and J. W. Freeland, *Physical Review Letters* **107**, 116805 (2011).
 - [6] W. R. L. Lambrecht, *physica status solidi (b)* **248**, 1547 (2011).
 - [7] C. W. M. Castleton, A. Hglund, and S. Mirbt, *Modelling and Simulation in Materials Science and Engineering* **17**, 084003 (2009).
 - [8] G. Makov and M. C. Payne, *Phys. Rev. B: Condens. Matter* **51**, 4014 (1995).
 - [9] P. A. Schultz, *Physical Review Letters* **96**, 246401 (2006).
 - [10] J. P. Perdew and Y. Wang, *Phys. Rev. B* **45**, 13244 (1992).
 - [11] S. Lany and A. Zunger, *Phys. Rev. B* **78**, 235104 (2008).
 - [12] P. Deak, A. Gali, B. Aradi, and T. Frauenheim, *Phys. Status Solidi B* **248**, 790 (2011).
 - [13] R. Ramprasad, H. Zhu, P. Rinke, and M. Scheffler, *Physical Review Letters* **108**, 066404 (2012).
 - [14] T. M. Henderson, A. F. Izmaylov, G. Scalmani, and G. E. Scuseria, *J. Chem. Phys.* **131**, 044108 (2009), specifically, the HSEh parameterization of HSE06[52], called by the GAUSSIAN keyword HSEh1PBE.
 - [15] A. Janotti, J. B. Varley, P. Rinke, N. Umezawa, G. Kresse, and C. G. Van de Walle, *Phys. Rev. B* **81**, 085212 (2010).
 - [16] H.-P. Komsa, P. Broqvist, and A. Pasquarello, *Physical Review B* **81**, 205118 (2010).
 - [17] H.-P. Komsa and A. Pasquarello, *Phys. Rev. B: Condens. Matter Mater. Phys.* **84**, 075207/1 (2011).
 - [18] T. M. Henderson, J. Paier, and G. E. Scuseria, *Phys. Status Solidi B* **248**, 767 (2011).
 - [19] B. G. Janesko, T. M. Henderson, and G. E. Scuseria, *Phys. Chem. Chem. Phys.* **11**, 443 (2009).
 - [20] T. M. Henderson, A. F. Izmaylov, G. E. Scuseria, and A. Savin, *J. Theor. Comput. Chem.* **4**, 1254 (2008).
 - [21] M. J. Lucero, T. M. Henderson, and G. E. Scuseria, *J. Phys. Condens. Matter* **24**, 145504 (2012).
 - [22] F. El-Mellouhi, E. N. Brothers, M. J. Lucero, and G. E. Scuseria, *Phys. Rev. B* **84**, 115122 (2011).
 - [23] A. Janotti, D. Steiauf, and C. G. Van de Walle, *Phys. Rev. B* **84**, 201304 (2011).
 - [24] B. Jalan, S. J. Allen, G. E. Beltz, P. Moetaf, and S. Stemmer, *Appl. Phys. Lett.* **98**, 132102/1 (2011).
 - [25] R. Wahl, D. Vogtenhuber, and G. Kresse, *Phys. Rev. B* **78**, 104116/1 (2008).
 - [26] F. El-Mellouhi, E. N. Brothers, M. J. Lucero, I. W. Bulik, and G. E. Scuseria, *Phys. Rev. B* **87**, 035107 (2013).
 - [27] J. Hong, G. Catalan, J. F. Scott, and E. Artacho, *J. Phys.: Condens. Matter* **22**, 112201/1 (2010).
 - [28] R. A. Evarestov, E. Blokhin, D. Gryaznov, E. A. Kotomin, and J. Maier, *Phys. Rev. B* **83**, 134108 (2011).
 - [29] P. García-Fernández, S. Ghosh, N. J. English, and J. A. Aramburu, *Phys. Rev. B* **86**, 144107 (2012).
 - [30] Y. F. Zhukovskii, E. A. Kotomin, S. Piskunov, and D. E. Ellis, *Solid State Commun.* **149**, 1359 (2009).
 - [31] M. J. Frisch, G. W. Trucks, G. E. Schlegel, H. B. and Scuseria, M. A. Robb, J. R. Cheeseman, G. Scalmani, V. Barone, B. Mennucci, G. A. Peters-

- son, H. Nakatsuji, M. Caricato, X. Li, H. P. Hratchian, A. F. Izmaylov, J. Bloino, G. Zheng, J. L. Sonnenberg, M. Hada, M. Ehara, K. Toyota, R. Fukuda, J. Hasegawa, M. Ishida, T. Nakajima, Y. Honda, O. Kitao, H. Nakai, T. Vreven, J. A. Montgomery, Jr., J. E. Peralta, F. Ogliaro, M. Bearpark, J. J. Heyd, E. Brothers, V. N. Kudin, K. N. and Staroverov, R. Kobayashi, J. Normand, K. Raghavachari, A. Rendell, J. C. Burant, S. S. Iyengar, J. Tomasi, M. Cossi, N. Rega, J. M. Millam, M. Klene, J. E. Knox, J. B. Cross, V. Bakken, C. Adamo, J. Jaramillo, R. Gomperts, R. E. Stratmann, O. Yazyev, A. J. Austin, R. Cammi, C. Pomelli, R. L. Ochterski, J. W. and Martin, K. Morokuma, V. G. Zakrzewski, G. A. Voth, P. Salvador, J. J. Dannenberg, S. Dapprich, A. D. Daniels, O. Farkas, J. B. Foresman, J. V. Ortiz, J. Cioslowski, and D. J. Fox, "Gaussian development version, revision h.11,".
- [32] K. N. Kudin and G. E. Scuseria, Phys. Rev. B **61**, 16440 (2000).
- [33] J. P. Perdew, K. Burke, and M. Ernzerhof, Phys. Rev. Lett. **77**, 3865 (1996).
- [34] J. P. Perdew, K. Burke, and M. Ernzerhof, Phys. Rev. Lett. **78**, 1396 (1997).
- [35] F. Weigend and R. Ahlrichs, Phys. Chem. Chem. Phys. **7**, 3297 (2005).
- [36] ICSD, "Inorganic Crystallographic Structural Database," www.fiz-karlsruhe.de/icsd_web.html (2010), specifically, the ICSD collection ID numbers are: bulk Sr (FCC), bulk Ti (hcp) SrO (Fm3m) 109461, TiO (Fm3m) 40125, Ti₂O₃ (R3C) 1462, Ti₂O(P4₂/mmm).
- [37] S. Piskunov, E. Heifets, R. I. Eglitis, and G. Borstel, Comput. Mater. Sci. **29**, 165 (2004).
- [38] K. van Benthem, C. Elsasser, and R. H. French, J. App. Phys. **90**, 6156 (2001).
- [39] Y. A. Abramov, V. G. Tsirelson, V. E. Zavodnik, S. A. Ivanov, and I. D. Brown, Acta Crystallographica Section B **51**, 942 (1995).
- [40] K. H. Hellwege and A. M. Hellwege, "Ferroelectrics and related substances, landolt-börnstein, new series, group iii," (Springer Verlag, Berlin, 1969).
- [41] S. B. Zhang and J. Northrup, Phys. Rev. Lett. **67**, 2339 (1993).
- [42] T. Tanaka, K. Matsunaga, Y. Ikuhara, and T. Yamamoto, Phys. Rev. B **68**, 205213 (2003).
- [43] W. G. Mallard and T. D. Linstrom, eds., NIST Chemistry WebBook, NIST Standard Reference Database, Vol. 69 (National Institute of standards and Technology, Gaithersburg, MD).
- [44] Point A: $\mu_{\text{O}} = \mu_{\text{O}}(\text{bulk}), \mu_{\text{Sr}} + \mu_{\text{O}} = \mu_{\text{SrO}}(\text{bulk})$ where $\mu_{\text{O}}(\text{bulk})$ corresponding to the chemical potential per atom of O₂ gas.
Point B: $\mu_{\text{O}} = \mu_{\text{O}}(\text{bulk})$, $\mu_{\text{Ti}} + 2\mu_{\text{O}} = \mu_{\text{TiO}_2}(\text{bulk})$.
Point C: $\mu_{\text{Ti}} + 2\mu_{\text{O}} = \mu_{\text{TiO}_2}(\text{bulk})$,
 $2\mu_{\text{Ti}} + 3\mu_{\text{O}} = \mu_{\text{Ti}_2\text{O}_3}(\text{bulk})$.
Point D: $\mu_{\text{Ti}} + \mu_{\text{O}} = \mu_{\text{TiO}}(\text{bulk})$,
 $2\mu_{\text{Ti}} + 3\mu_{\text{O}} = \mu_{\text{Ti}_2\text{O}_3}(\text{bulk})$.
Point E: $\mu_{\text{Ti}} + \mu_{\text{O}} = \mu_{\text{TiO}}(\text{bulk})$, $\mu_{\text{Ti}} = \mu_{\text{Ti}}(\text{bulk})$
Point F: $\mu_{\text{Ti}} = \mu_{\text{Ti}}(\text{bulk})$, $\mu_{\text{Sr}} = \mu_{\text{Sr}}(\text{bulk})$
Point G: $\mu_{\text{Sr}} = \mu_{\text{Sr}}(\text{bulk})$, $\mu_{\text{Sr}} + \mu_{\text{O}} = \mu_{\text{SrO}}(\text{bulk})$.
- [45] J. Carrasco, F. Illas, N. Lopez, E. A. Kotomin, Y. F. Zhukovskii, R. A. Evarestov, Y. A. Mastrikov, S. Piskunov, and J. Maier, Physical Review B **73**, 064106 (2006).
- [46] W. Luo, W. Duan, S. G. Louie, and M. L. Cohen, Physical Review B **70**, 214109 (2004).
- [47] W. Wunderlich, H. Ohta, and K. Koumoto, Physica B: Condensed Matter **404**, 2202 (2009).
- [48] M. Marques, L. K. Teles, V. Anjos, L. M. R. Solfaro, J. R. Leite, V. N. Freire, G. A. Farias, and da Silva E. F. Jr, Appl. Phys. Lett. **82**, 3074 (2003).
- [49] D. Kan, T. Tetashima, R. Kanda, A. Masuno, K. Tanaka, S. Chu, H. Kan, A. Ishizumi, Y. Kanemitsu, Y. Shimakawa, and M. Takano, Nat Mater **4**, 816 (2005).
- [50] M. I. J. Probert and M. C. Payne, Phys. Rev. B **67**, 075204 (2003).
- [51] P. Deak, B. Aradi, T. Frauenheim, E. Janzen, and A. Gali, Phys. Rev. B. **81**, 153203/1 (2010).
- [52] J. Heyd, G. E. Scuseria, and M. Ernzerhof, J. Chem. Phys. **124**, 219906 (2006).